Interaction mechanisms in small-scale model MSE walls under the strip footing load

H. Ahmadi[1], A. Bezuijen[2] and J.G. Zornberg[3]

[1] *PhD graduate student, Ghent University, Department of Civil Engineering, Laboratory of Geotechnics, Technologiepark 905, B-9052 Gent, Belgium, E-mail: hamzeh.ahmadi@gmail.com (corresponding author)*
[2] *Professor, Ghent University, Department of Civil Engineering, Laboratory of Geotechnics, Technologiepark 905, B-9052 Gent, Belgium; Deltares, Delft, The Netherlands, E-mail: adam.bezuijen@ugent.be*
[3] *Professor, The University of Texas at Austin, Department of Civil, Architectural and Environmental Engineering, Austin, TX, 78712, USA, E-mail: zornberg@mail.utexas.edu*

Received 11 September 2019, revised 20 May 2020, accepted 14 August 2020, published 08 January 2021

ABSTRACT: The effect of preloading on mechanically stabilised earth (MSE) has remained an aspect difficult to quantify in design, particularly when considering different reinforcement types, stiffness values, and facing rigidity. This study analyses several scaled model tests on MSE walls under a strip footing load with a single unloading-reloading cycle. Scaled models were constructed as part of this investigation to expand the evaluation of previously constructed full-scale tests. The strip footing load and wall deflections were measured and compared with analytical models. The failure mechanism of the soil, before and after the strip footing load, was included in the study via the particle image velocimetry (PIV) method. The results indicate that the bearing capacity of a strip footing is higher for a rigid facing than for a flexible facing. PIV analysis results for the first and second loading step formed two failure lines with the angle ($\pi/4 + \varphi/2$). The deflection values in the second loading step, however, were smaller than those reached during the first loading in small-scale tests. Good agreement was observed between the proposed analytical method and experimental results for the second loading step, after taking into account the preloading effect.

KEYWORDS: Geosynthetics, Scaled MSE model tests, Strip footing load, Preloading, Analytical analysis, Particle image velocimetry (PIV)

REFERENCE: Ahmadi, H., Bezuijen, A. and Zornberg, J.G. (2021). Interaction mechanisms in small-scale model MSE walls under the strip footing load. *Geosynthetics International*, **28**, No. 3, 238–258. [https://doi.org/10.1680/jgein.20.00040]

1. INTRODUCTION

In many situations, footings are located on the backfill of retaining structures (e.g. footings on bridge abutments or roads located on top of the retaining structure). The behaviour of reinforced earth structures under a strip footing load has been studied through full-scale physical models and laboratory model tests (Adams 1997; Gotteland *et al.* 1997; Ketchart and Wu 1997; Wu *et al.* 2001; Abu-Hejleh *et al.* 2002; Lee and Wu 2004; Adams *et al.* 2011; Bourgeois *et al.* 2011; Ahmadi and Hajialilue-Bonab 2012; Allen and Bathurst 2015; Xiao *et al.* 2016; Ahmadi and Bezuijen 2018; Allen and Bathurst 2019; Zornberg *et al.* 2019; Bathurst 2020).

For a footing constructed behind a reinforced earth wall, the maximum bearing capacity will depend on a number of factors (Ahmadi and Hajialilue-Bonab 2012 and Xiao *et al*. 2016), including: (1) the location of the footing in relation to the wall; (2) the type of reinforcement; (3) the number of reinforcement layers; (4) the depth to the first reinforcement layer below the footing; (5) the spacing between reinforcement layers; and (6) the dimensions of the reinforcement, as compared with the dimensions of the wall.

A recent study by Ahmadi and Bezuijen (2018) showed that facing panel rigidity and base restriction can have a significant effect on wall deflections and loads in the reinforcement layers. Tatsuoka (1992) showed that the facing rigidity in reinforced soil walls has a significant effect on the distribution of tensile forces induced in the reinforcement without surcharge loading. In the Tatsuoka (1992) study, the largest tensile forces occurred close to the wall face for a reinforcement with good connection to a rigid facing, while the largest tensile forces were measured farther away from the wall face where there was no connection, or the connection force was small.

For reinforced soil walls only (without a strip footing load), Ho and Rowe (1996) and Rowe and Ho (1997) found that reinforcement stiffness, vertical spacing and the length-to-wall-height ratio (L/H) are important parameters that affect wall displacement.

In MSE walls during compaction, unloading-reloading cycles occur as part of the backfill placement. This construction step decreases lateral wall deflections and settlements under subsequent surcharge loads. In reinforced soil retaining walls, the compaction loads increase the lateral earth pressures close to the facing panels. The increased lateral earth pressures are transferred to the reinforcement layers by frictional or bearing interaction mechanisms. The necessary deformation for mobilisation of the ultimate frictional and bearing resistance in geosynthetic (extensible) material is also comparatively large (Teixeira *et al*. 2007).

Consequently, the reinforcement layers elongate under the added compaction-induced lateral earth pressures. The elongated reinforced layer remains in the pre-stressed condition after removing compaction loads as the increased soil densification prevents stress relieving (Lackner *et al*. 2013). This phenomenon has been considered to improve the deformation characteristics of the MSE walls or bridge abutments by applying static or dynamic loads as a preloading surcharge to mobilise the reinforcement layers within the soil mass by prestressing them. The approach is expected to result in comparatively smaller wall deflections and footing settlements under subsequently applied surcharge loads. A related experience was reported by Ahmadi and Bezuijen (2018), which involved localised dynamic preloading before the subsequent static loading with a strip footing placed over full-scale MSE walls. The results showed that without preloading, the lateral wall deflections were essentially twice those obtained when considering a dynamic preloading.

The location of maximum tensile loads is a key assumption in the design of geosynthetic reinforced soil wall systems loaded with strip footings. The AASHTO (2012) design method considers that the locus of maximum tensile forces starts at the wall toe and shifts to intersect the back of the footing at the top of the wall (e.g. a bridge seat). The maximum tensile force in each reinforcement layer is calculated along the failure surface using empirical approaches such as the 2V:1H method. However, the impact on this locus on variables such as reinforcement characteristics, reinforcement spacing, facing rigidity, and preloading requires further investigation.

Specifically, limited research has been conducted on the behaviour of mechanically stabilised earth (MSE) walls under a strip footing load considering different reinforcement layer stiffnesses and types, different facing panel rigidities and preloading effects.

Furthermore, for these types of structures, limited experimental data sources exist that evaluate changes in failure mechanism when the facing panel rigidity and reinforcement types are varied under a single unloading-reloading cycle.

This paper presents a series of instrumented reduced-scale models, the evaluation of which is useful to assess the influence of facing panel rigidity, the stiffness of the reinforcement layers and preloading on lateral wall deflections, strip footing settlements, vertical earth pressures and, consequently, the maximum tensile force in the reinforcement layers. The effects of dynamic or static loading to improve subsurface soils by increasing their density and/or horizontal stresses are identified herein as the preloading effect.

2. EXPERIMENTAL SET-UP

2.1. Model box and wall

A series of experiments were conducted in a stiff metal test box with inner dimensions of 1 m in length, 0.8 m in width and 1 m in height. One side of the test box consisted of 30 mm-thick toughened glass (with a tensile strength of 65 MPa) for observing and photographing the soil deformation during testing (see Figure 1a). To minimise friction between the sidewalls of the box and backfill, several layers of thin, lubricated transparent plastic film were carefully installed to essentially isolate the soil mass from any frictional effects of the test box. The results of direct shear testing between sand and glass showed a friction angle of only 7.8°. The box was sufficiently rigid to maintain plane strain conditions in the reinforced retaining wall model. All tests were conducted with a wall height of 0.8 m and a reinforcement length of 0.6 m. A smooth wooden plate was placed at the bottom of the box. Accordingly, the friction between the facing panel and base plate of the box was minimised in the small-scale tests (on the other hand, based on the numerical analysis results, the toe friction coefficient was considered as 0.2 in order to get the same wall movement in the base for the test and numerical analysis).

The test configurations are given in Figure 1b. Three different types of reinforcements (geogrid, nonwoven and woven geotextiles) and two types of facing panels (full height rigid and flexible panel) were used in the tests. The flexible and rigid facing panels consisted of 3 mm-thick and 50 mm-thick factory plywood plates, respectively ($EI = 28 \times 10^{-3}$ and 130 kN.m^2/m, respectively). Four linear variable displacement transducers (LVDTs) were used to measure the horizontal displacements of the wall.

2.2. Strip footing model and loading system

The strip footing was made of steel welded plates in a channel shape with a length of 0.795 m, a width of 0.2 m, a height of 0.15 m and a thickness of 0.025 m ($EI = 6.2 \times 10^3$ kN.m^2). The length of the footing and width of the test box were made to be nearly equal to maintain plane strain conditions. The two ends of the footing plate were covered with smooth plastic to minimise end friction effects. After filling the box with compacted sand, the surface of the sand was levelled, and the model footing was placed on the predetermined

(a)

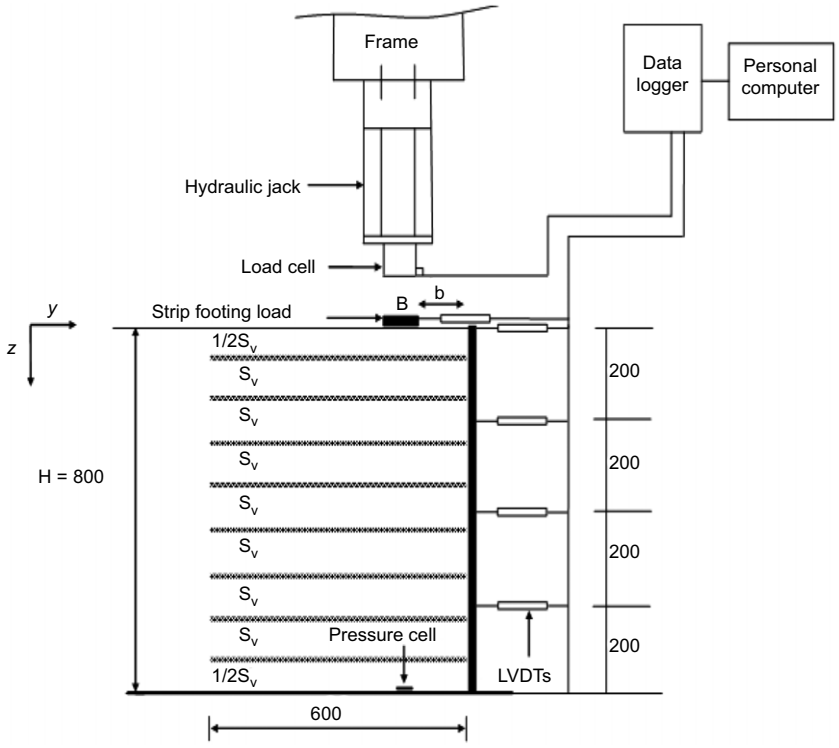

(b)

Figure 1. Test layout for reinforced soil wall and parameter symbols (dimensions in mm)

location. A 100 kN load cell placed between the hydraulic jack and reaction beam recorded the magnitude of loads applied to the footing at a constant displacement rate. The load from the hydraulic jack was transferred concentrically to the footing. A pressure gauge 200 mm in diameter (for vertical stress measurements) was placed horizontally at $z = 0.8$ m in the centreline of the strip footing on the bottom of the container (see Figure 1b). The vertical displacements of the model footing were measured by two LVDTs located at the front and centreline of the strip footing. To study the effects of preloading and pre-stressed conditions on the models, a reloading step was applied in every test to the strip footing load following the first load. In the model tests, after unloading of the strip footing load, a second load (reloading) was applied to models, to study the effect of the preloading on the wall deflection under the strip footing load. A cross-section is shown in Figure 1b.

2.3. Soil and reinforcement

The soil used in this study was a dry sand that classifies as SP (poorly graded sand) with no fines according to the Unified Soil Classification System (USCS). The particle size distribution was characterised via the dry sieving method and the results are presented in Figure 2. Because of inter-grain colour variation, images of the sand displayed a wide spectrum of intensity values. A favourable spatial distribution of brightness provided well-textured images for PIV analysis. Table 1 presents the properties of the sand. Soil layers were placed every 0.025 m and compacted by a hand-held electric compactor (Wacker) until the final wall height was achieved. The backfill soil for all tests was compacted using a small vibrating plate compactor, which provided a uniform backfill with an average unit weight of 15.72 kN/m^3 and a relative density of 88%. The friction angle obtained from direct shear tests at the same relative density of the model tests was 40.5°. Following soil compaction, reinforcements were placed on the surface of the sand at each predetermined depth. Three different types of reinforcements were used in this study, including a highly extensible nonwoven geotextile, a less deformable geogrid and a woven geotextile. Tensile tests were conducted on the specimens in the longitudinal direction and the results are given in Figure 3. The properties of the reinforcements selected are shown in Table 1. The stiffness of the geogrid layer used in the models is 1/5 of that used in the full-scale reinforced soil structures reported by Ahmadi and Bezuijen (2018). On the other hand, the stiffness of woven geotextiles is similar to the geogrid reinforcements in the small-scale models. Finally, the stiffness of the nonwoven geotextile was 10 times smaller than the geogrid layers used in the small-scale models to reach the ultimate bearing capacity of the strip footing load.

2.4. Model characteristics

A series of tests were conducted in which the number and vertical spacing of the reinforcement layers (N and S_v),

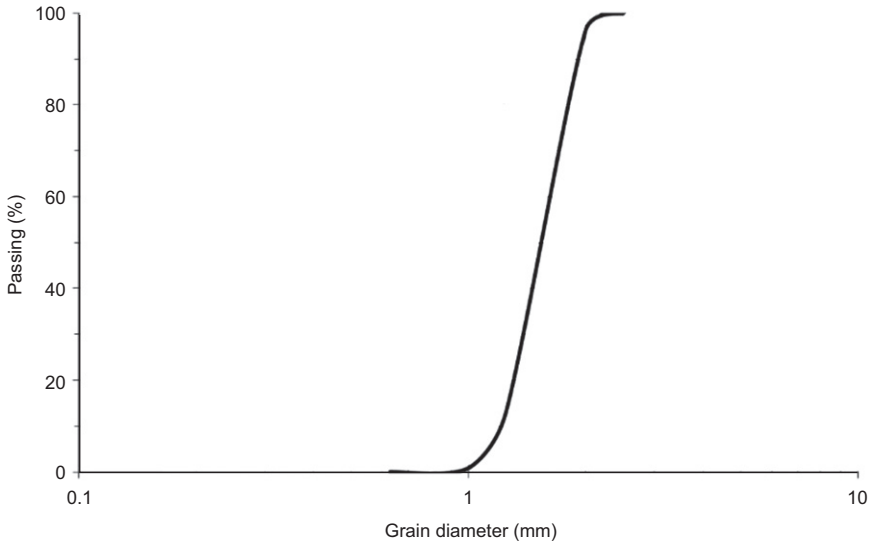

Figure 2. Grain size distribution of the sand used in this investigation

Table 1 Soil and reinforcement parameters in scaled tests

Parameter	Symbol	Value
Unit weight-soil (kN/m^3)	γ_s	15.72
Coefficient of uniformity	C_u	1.32
Coefficient of curvature	C_c	0.96
Peak soil friction angle from the direct shear test (°)	φ_d	40.5
Residual friction angle from the direct shear test (°)	φ_r	31.15
Estimated soil plain strain friction angle (Bolton 1986) (°)	φ_p	46
Cohesion-soil (kPa)	C	0
Reinforcement length (m)	L	0.6
Vertical spacing of reinforcement in four layers (m)	S_v	0.1 and 0.2
Vertical spacing of reinforcement in eight layers (m)	S_v	0.05 and 0.1
Short term stiffness of geogrid ($\varepsilon \leq 4\%$) (kN/m),	E_1A	150
Ultimate tensile strength (kN/m)	T_{u1}	10
Short term stiffness of woven geotextile ($\varepsilon \leq 4\%$) (kN/m)	E_2A	230
Ultimate tensile strength (kN/m)	T_{u2}	25
Short term stiffness of nonwoven geotextile ($\varepsilon \leq 40\%$) (kN/m)	E_3A	15
Ultimate tensile strength (kN/m)	T_{u3}	8

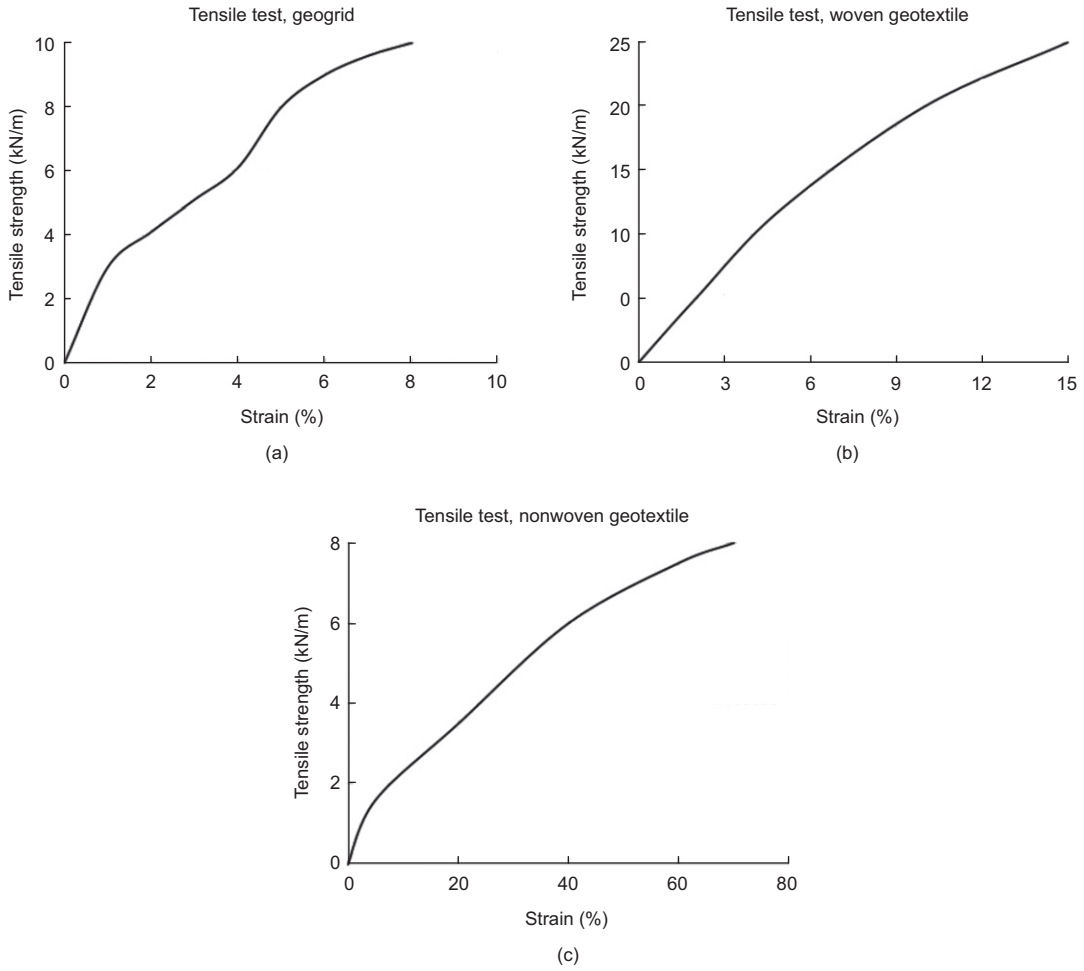

Figure 3. Tensile load test results until the maximum value: (a) geogrid; (b) woven geotextile and (c) nonwoven geotextile

reinforcement type and wall facing panel rigidity were varied, while the distance of the strip footing from the wall face (b), length of the reinforcement layers (L) and width of the strip footing load (B) were fixed. Table 2 summarises the various test conditions. Additional parameters were adopted to define the facing panel rigidity and loading steps for the reinforced soil models: F and R represent the flexible and rigid faces, respectively, and 1 and 2 represent the first loading and second loading step, respectively.

Table 2. Laboratory model test conditions

Test	N	u/B	h/H	b/B	L/H
Four layers-nonwoven-F-1 Four layers-nonwoven-R-1	4	0.25	0.25	0.5	0.75
Four layers-woven-F-1,2 Four layers-woven-R-1,2	4	0.25	0.25	0.5	0.75
Four layers-geogrid-F-1,2 Four layers-geogrid-R-1,2	4	0.25	0.25	0.5	0.75
Eight layers-nonwoven-F-1 Eight layers-nonwoven-R-1,2	8	0.5	0.125	0.5	0.75
Eight layers-woven-F-1,2 Eight layers-woven-R-1,2	8	0.5	0.125	0.5	0.75

3. TYPES OF FAILURE IN SOIL UNDER STRIP FOOTING LOAD

According to Plumey *et al.* (2011) and Ahmadi and Hajialilue-Bonab (2012), the failure mechanism in the soil for a flexural retaining structure fixed to the base and linear footing is composed of a rigid body and plasticised (or shear) area delimited by logarithmic spirals. The critical slip surface of a MSE wall divides the reinforced zone into an active and a resistant zone. The reinforcement lengths within the resistant zone provide pull-out resistance and the shear stresses in the active zone are directed outward and lead to a decrease in tensile forces. The critical slip surface in a reinforced soil wall is assumed to coincide with the maximum tensile force line in the failure step. In conventional MSE walls, the location of maximum tensile force depends primarily on the type of reinforcement used. In the case of inextensible reinforcements, the failure surface is assumed to be approximately bilinear and varies with depth. In the case of extensible reinforcements, the maximum tensile force surface is assumed to be approximately linear and to pass through the toe of the wall (FHWA 2009).

In the case of MSE abutments, it has been observed that the locus of maximum tensile loads in the geotextiles may change depending mainly on the geometry of the footing

(Schlosser and Bastick 1991; Brabant 2001). The location of maximum tensile forces shifts to intersect the back of the bridge seat and wall toe based on the strip footing locations.

3.1. Digital imaging and PIV method

Using the PIV method as implemented by the image processing software GeoPIV (White *et al*. 2001, 2003, 2005), successive pairs of photographs were compared to determine incremental displacement and strain values. A Panasonic Lumix DMC-GH3 (16.1 megapixel) camera, positioned in front of the sidewall of the test box, facilitated visualisation of soil movement during testing and image processing. All controls, such as focus, gain and shutter speed, were automatically adjusted. Two projectors positioned on both sides of the camera at 45° angles and one positioned above the camera's optical axis eliminated optical effects from the environment on the viewing window, thereby preventing errors caused by random variation in pixel intensity. The first step in PIV analysis is to divide the digital image into square patches of pixels to form a regular mesh. Because PIV precision is a function of patch size and grid spacing, an initial study of convergence and stability was performed using different patch sizes and grid spacings. According to Lesniewska and Wood (2009), Ahmadi and Hajialilue-Bonab (2012) and Ahmadi (2020), if the patch is too small, the amount of information captured may not allow the software to recognise the displaced patch with confidence, which may yield false displacement values. The next quantity that must be defined is the grid spacing used for successive displacement estimates within each image. Strain calculations require the differentiation of displacement information. A finer grid implies greater detail, but also a greater probability of erratic values. Consequently, the selection of an optimum patch size in PIV analysis necessitates a balance between two conflicting interests. Larger patches offer improved precision, whereas smaller patches ensure a greater number of measurement points in the image and reveal detail in areas with a high strain gradient. The best solution that provides a compromise between these problems is the use of relatively large, overlapping patches.

The displacement fields obtained for three different reinforcements are shown in Figure 4 (the PIV analysis was conducted with a patch size of 64 × 64 pixels and a mesh spacing of 64). Soil tended to move toward the wall, with a well-defined failure zone in all cases. As depicted in the figure, the failure zone for the flexible reinforcement (nonwoven geotextile) was deeper than for the woven geotextile and geogrid, and the model with the woven geotextile had the widest failure zone. In the model with the nonwoven geotextile, the first reinforcement layer visibly pulled away from the soil.

Figure 5 presents the total maximum shear strain distributions for the same tests shown in Figure 4. The PIV analysis was conducted with a patch size of 64 × 64 pixels and a mesh spacing of eight pixels in Figures 5–8 (containing 102,543 patches and 232,766 elements).

The same range of total maximum shear strain (0–30%) is plotted for all cases to facilitate a comparison of the results (strain localisation in these and other pictures clearly indicates where the failure occurred in the soil).

This figure shows the effect of changing the reinforcement type while maintaining equal vertical displacement steps in the shear zones. The failure patterns in Figures 5a–5c are straight lines. There is a clear triangular failure shape in Figure 5c as well as under the strip footing for the geogrid reinforcement. The failure lines in Figure 5 are delineated by white dashed lines having an angle $(\pi/4 + \varphi/2)$ with the horizontal.

Two main failure lines with a tendency to move toward the wall are created in Figures 5b and 5c: one with a shallow position and one with a deep position. These lines have the angle $(\pi/4 + \varphi/2)$, but with different failure depths and originations. Figures 5a and 5b have deeper failure lines compared to Figure 5c. This indicates that the failure zone is deeper for the geotextile reinforcements with frictional interaction only than for the geogrid with smaller frictional and larger bearing interaction (the geogrid and woven geotextile have a 35% difference in stiffness).

Considering the interaction phenomena between the reinforcements and soil displayed in these figures, the interacted area in the nonwoven geotextile (Figure 5a) was limited around the failure line with the angle $(\pi/4 + \varphi/2)$, but for the woven geotextile (Figure 5b), this area continued to the end of the reinforcement layers.

The total maximum shear strains shown in Figures 6a–6c indicate different failure mechanisms for reinforced models with a rigid face. Figures 6a–6c display shear failures for configurations with a rigid wall that included nonwoven and woven geotextiles, and geogrid reinforcement layers, respectively. The first reinforcement layer in all figures was pulled away from the soil. The failures involving the nonwoven geotextile and geogrid layers were small and shallow, located over the third reinforcement layer. For the woven geotextile layers (Figure 6b), the failure zones were larger and deeper than in Figures 6a and 6c. Additionally, an incomplete shallow failure line over the second layer can be seen in Figure 6b. The data presented in Figures 5 and 6 reveal that the woven geotextile with greater stiffness exhibited a deeper failure line of the models than the nonwoven geotextile with more frictional interaction and the geogrid reinforcement.

As shown in Figure 6, two failure lines with the angle $(\pi/4 + \varphi/2)$ formed: one from the inner edge of the strip footing, with a tendency toward the wall face (shallow position), and another from the outer edge of the strip footing (deep position). A comparison of Figures 5 and 6 indicates that the failure zones were deeper in the rigid wall models compared to the failure zones measured in the flexible wall models with the woven geotextile and geogrid reinforcement. The vertical failure line close to the wall face in these figures shows the frictional interaction between the face and soil. This vertical line is clear for the rigid wall in Figure 6. The combination of deeper failure line (with the angle $(\pi/4 + \varphi/2)$) and triangular failure

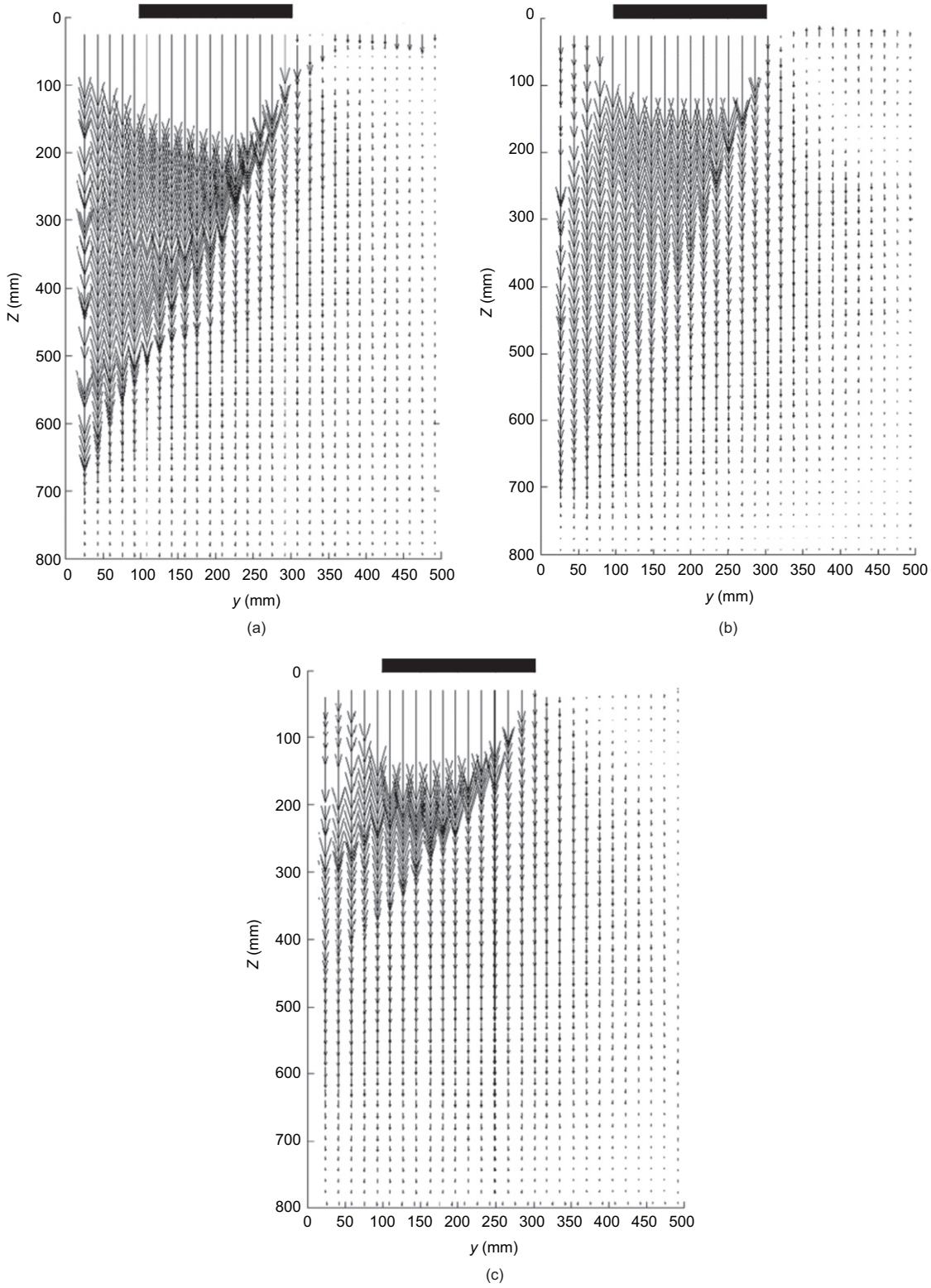

Figure 4. Displacement fields obtained by PIV analysis for reinforced backfill with four layers and flexible face ($dz = 0.08B$): (a) nonwoven geotextile; (b) woven geotextile; and (c) geogrid

shape under the strip footing load in the rigid wall exhibited the higher ultimate bearing capacity.

Figure 7 shows shear strains with a 64 × 64 pixel patch size and mesh spacing of eight pixels (the optimal patch size and mesh spacing established). Increasing the mesh refinement revealed shear strain maps that divided into several distinct zones. Shear strain zones that occurred between every step of the footing settlement were inspected using the incremental maximum shear strains (IMSS), which are based on PIV analysis results. This figure presents the results of a test in which eight nonwoven geotextile layers and a flexible facing panel were used. Step 1 in Figure 7 shows shear zones after the struts in front of the wall were released, which occurred at

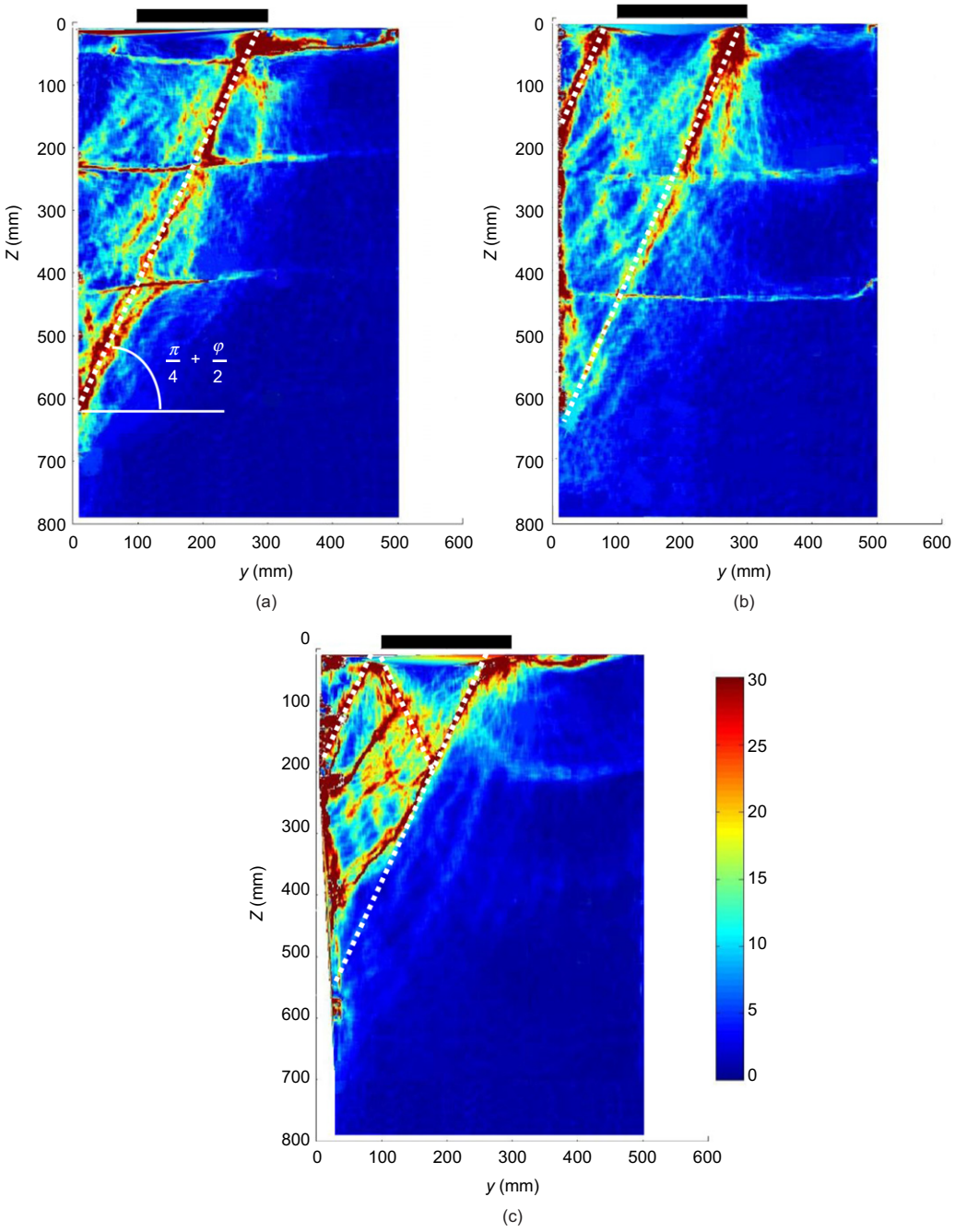

Figure 5. Total maximum shear strains obtained from PIV data for reinforced backfill with four layers and flexible face ($dz = 0.08B$): (a) nonwoven geotextile; (b) woven geotextile; and (c) geogrid

a strain range of 0–10%. Small strains that occurred between reinforcement layers were situated lower, as seen in this figure, revealing the confinement effect of the reinforcement layers in the horizontal direction (Ruiken *et al*. 2010). In steps 2 (after first loading) and 3 (after unloading), two straight failure lines emerged, originating from the outer and inner edges of the footing, with the angle ($\pi/4 + \varphi/2$), as delineated by the white dashed lines. The failure line from the outside of the footing was deeper than the inner failure line. In step 2, over the second layer of reinforcement, there was a failure zone similar to the general shear failure. Complete general shear failure occurred in step 4 (after reloading the sample) and causes a rotational movement in the strip footing (which shows that the applied pressure is close to the ultimate bearing capacity of the strip footing).

Figure 8 shows four steps of a test with eight layers of nonwoven geotextile and the rigid wall that contain the shear zones from the IMSS output. In step 1 of this figure, there are small shear zones between the reinforcement layers that occurred in the higher position of the wall (compared to Figure 7).

In steps 2, 3 and 4, only a straight failure line emerged starting from the outside edge of the footing with the angle ($\pi/4 + \varphi/2$). In these steps, and over the second layer of reinforcement, there is an incomplete failure zone similar to the general shear failure and smaller than the zone shown in Figure 7. In this step, the strip footing

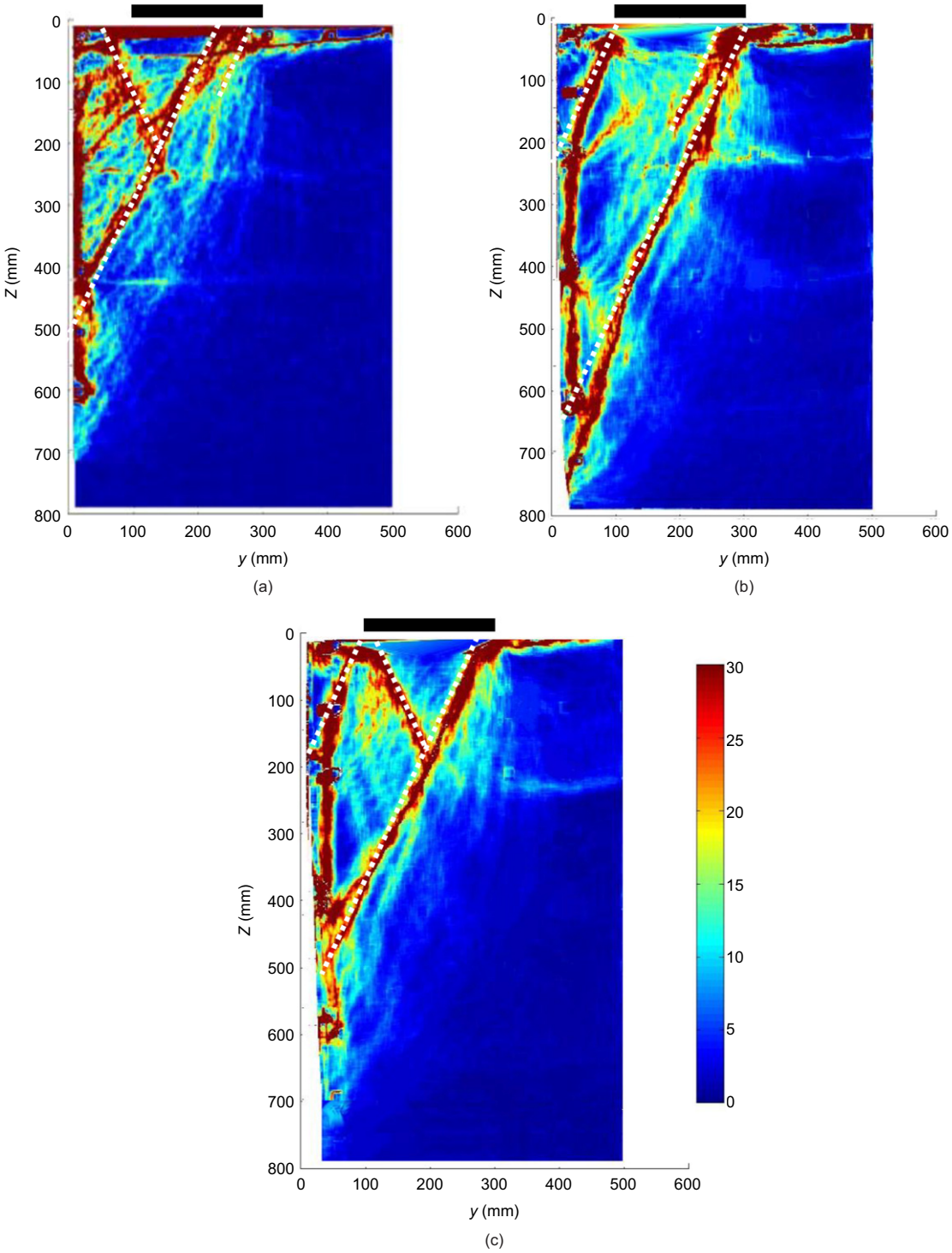

Figure 6. Total maximum shear strains obtained from PIV data for reinforced backfill with four layers and rigid face ($d_z = 0.08B$): (a) nonwoven geotextile; (b) woven geotextile; and (c) geogrid

remained horizontal (showing that the applied pressure is smaller than the ultimate bearing capacity of the strip footing). In the rigid wall, compared to the flexible wall, there is a clear failure line generated between the soil and wall face in the vertical direction (soil-wall face frictional interaction).

From the PIV analysis results of Ahmadi and Hajialilue-Bonab (2012), for the flexural retaining structure fixed in the base, the failure mechanism in the soil was composed of two logarithmic spirals, but from this study for the MSE walls with flexible and rigid faces, the failure zone has two main lines with the angle ($\pi/4 + \varphi/2$). Then, the base fixation of the flexible facing panel can change the shape of the failure zones from a linear to a spiral shape.

On the other hand, compared to AASHTO (2012) (line of the maximum tension under the strip footing load close to the MSE walls), the experimental models of this study showed different failure lines for different facing panel and reinforcement types. The failure zone from PIV analysis

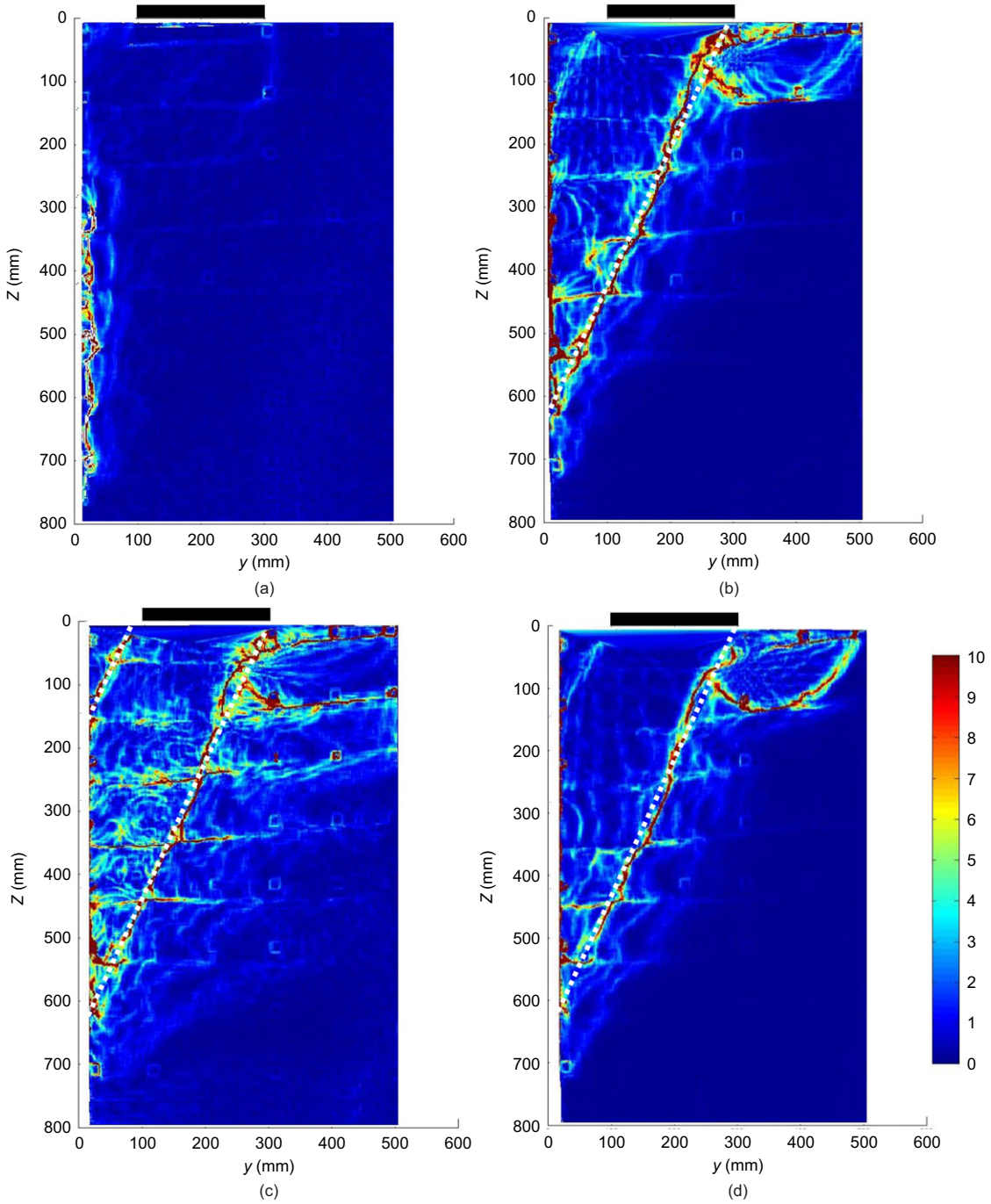

Figure 7. Creation of shear strain zones by strip footing and flexible facing panel, four test steps, eight layers nonwoven-F, plotted in the: (a) step 1, end of backfill construction step, after releasing struts in front of wall; (b) step 2, end of first loading step (dz = 0.08B); (c) step 3, unloading step; and (d) step 4, end of second loading step (dz = 0.04B)

not only has an intersection with the wall face in upper position than wall base but also there are two parallel failure lines under the strip footing load.

4. MEASUREMENTS AND COMPARISON WITH ANALYTICAL METHODS

4.1. Vertical earth pressure

The AASHTO (2012) method presented an empirical method to calculate the stresses in the soil near a vertical wall caused by a strip footing load. The vertical pressure as a function of depth behind the retaining structures is

$$\begin{cases} q_{\mathrm{v}} = \dfrac{q \cdot B}{B + \mathrm{z}}, & z < 2b \\ q_{\mathrm{v}} = \dfrac{q \cdot B}{B + 2b}, & z \geq 2b \end{cases} \tag{1}$$

where b, distance between the load and the wall; B, width of the strip load; z, vertical distance from the soil surface; q, strip footing load q_{v}, vertical stress in the depth due to the strip footing load.

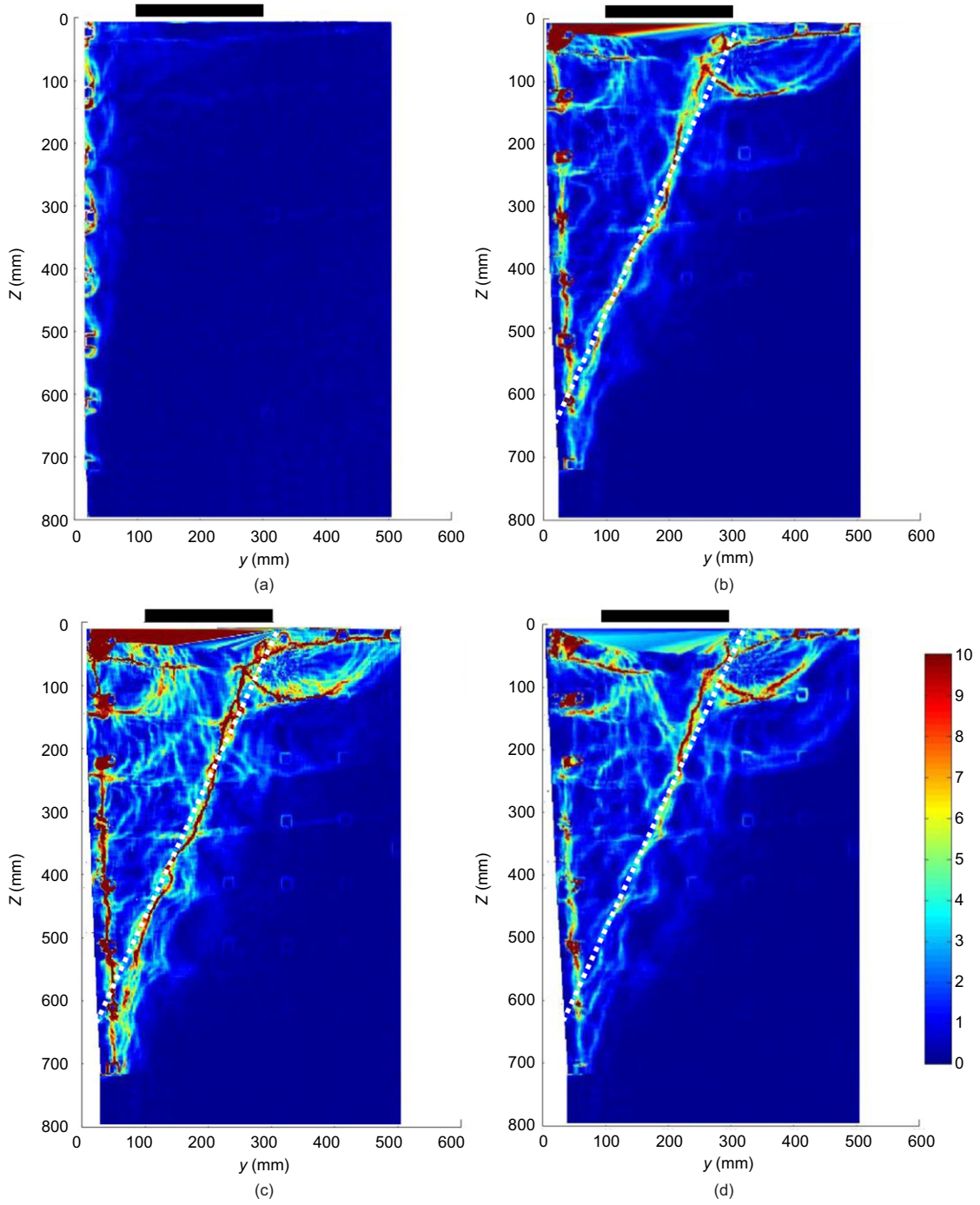

Figure 8. Creation of shear strain zones by strip footing and a rigid facing panel in face, four steps of test, eight layers nonwoven-R plotted at the end of: (a) end of backfill construction step and after releasing struts in front of the wall; (b) end of first loading steps ($dz = 0.08B$); (c) unloading step and (d) end of second loading step ($dz = 0.04B$)

Figure 9 compares the measurements of vertical earth pressure at different stages of loading with the AASHTO (2012) method and the empirical (2V:1H) method ($q_v = (q \cdot B)/B + z$). The vertical earth pressure is measured at the bottom of models during the first and second loading steps.

In Figure 9a with four layers of different types of reinforcement, the measured values are closer to the AASHTO (2012) method except for the rigid wall with nonwoven geotextile.

To clarify this phenomenon (as shown later in Figure 11), the largest wall deflection occurred on top of the rigid walls with nonwoven geotextile compared to others. However, the minimum wall movement occurred at the base of these two models. This suggests that the rigid face in these two models resulted in the largest rotation of the wall. Based on Coulomb's theory (Coulomb 1776), by increasing the facing panel inclination, a larger part of the lateral earth pressure will be carried by the facing panel due to friction interaction. This higher frictional load acts upward, decreasing the vertical soil pressure transferred to the base.

The measured values in the second loading of the models are shown in Figure 9b. The measured values are located

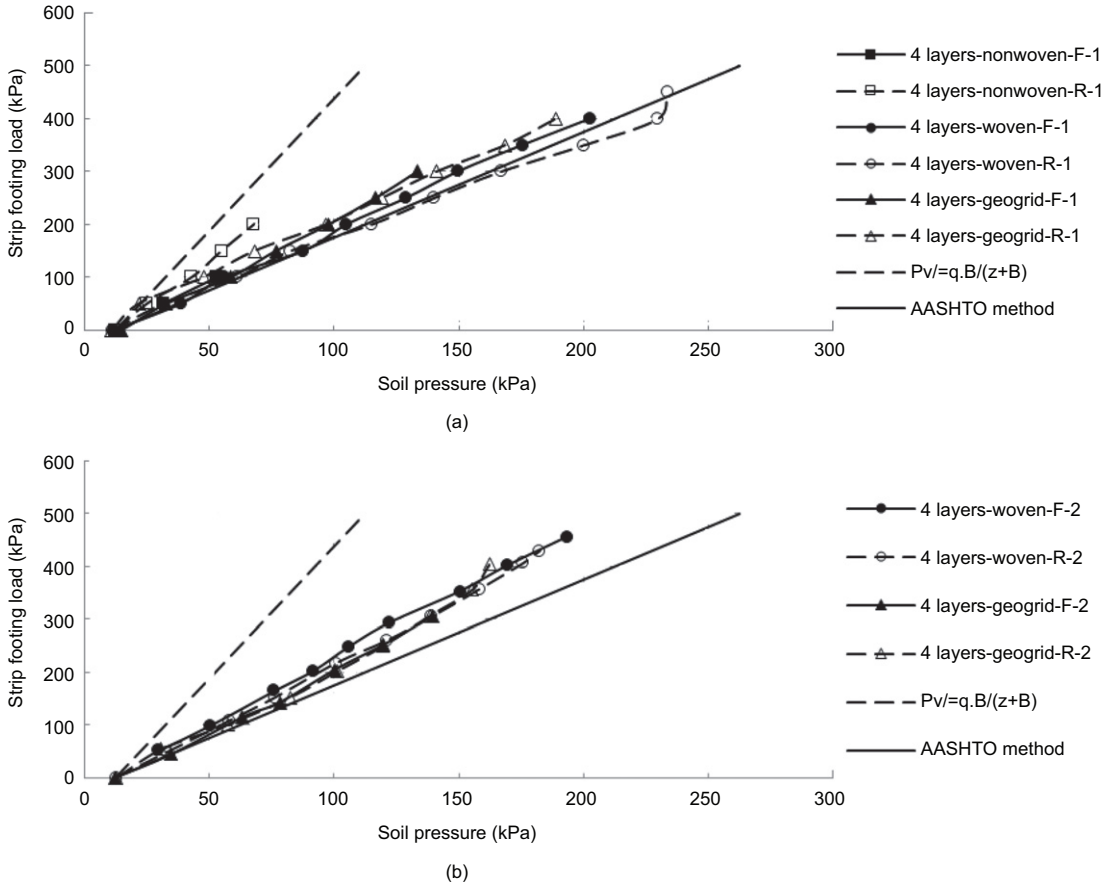

Figure 9. Vertical earth pressure distribution in the test and empirical methods after applying the strip footing load in rigid and flexible walls with four layers: (a) first loading step; (b) second loading step

between the empirical (2V:1H) method and the AASHTO (2012) method. It shows that by reloading the model, as there is a prestressed condition in reinforcement layers from the first loading step, less vertical soil pressure can be transferred to the base of the model from the facing panel.

On the other hand, Damians *et al*. (2014) showed that measured vertical loads at the toe of the facing panel can be much larger than the self-weight of the facing in MSE walls. This is most likely caused by the relative movement between the backfill soil and the panels that develops panel-soil interface shear and down drag loads at the connections between the panels and the reinforcement elements.

For the tests with four layers of nonwoven geotextile, as there was a failure with large lateral deformation, the second loading step was not considered. From Figure 9, the different loading states (loading and reloading), reinforcement types (stiffness) and facing panel rigidity can influence the vertical soil pressure distribution. As the facing panel rigidity increases, reinforcement layers stiffness decreases, or reloading states occurs, the vertical soil pressure decreases more than the calculated values from the AASHTO (2012) method.

4.2. Bearing capacity of strip footing load

Data from the load cell, the LVDTs fixed horizontally in front of the wall and over of the strip footing load were used to study the influence of the reinforcement layers on the bearing capacity of the footing and on the wall deflection.

Figure 10 shows the footing pressure versus the footing settlement (q–dz) and the footing pressure versus wall deflection (q–dy) in reinforced backfills and with different types of reinforcement layers.

By increasing the wall face rigidity and reinforcement stiffness, the bearing capacity of the strip footing increases and the wall deflection decreases. The results shown in Figures 5 and 6 help to interpret these phenomena: for a rigid face, a plastic area with a vertical line close to the facing panel occurred over the height of the panel, but for a flexible face, a plastic area with a shallow position formed.

As shown in Figure 10a, the ultimate bearing capacity of strip footing occurs in the model with nonwoven geotextiles at an approximate settlement of 0.08B. In addition, the effects of facing panel rigidity, reinforcement number, types and stiffness on reinforced fill were compared at this known settlement (0.08B).

The ultimate bearing capacity of a strip-footing load, based on an upper bound solution, can be written as (Sawicki and Lesniewska 1987)

$$P_{\mathrm{u}} = \sigma_0 \frac{b}{a} \tan^2\left(\frac{\pi}{4} + \frac{\varphi}{2}\right) - \frac{1}{2}\gamma H \tag{2}$$

where a, strip footing load width; b, the distance between the front wall and a farther edge of the footing; φ, soil

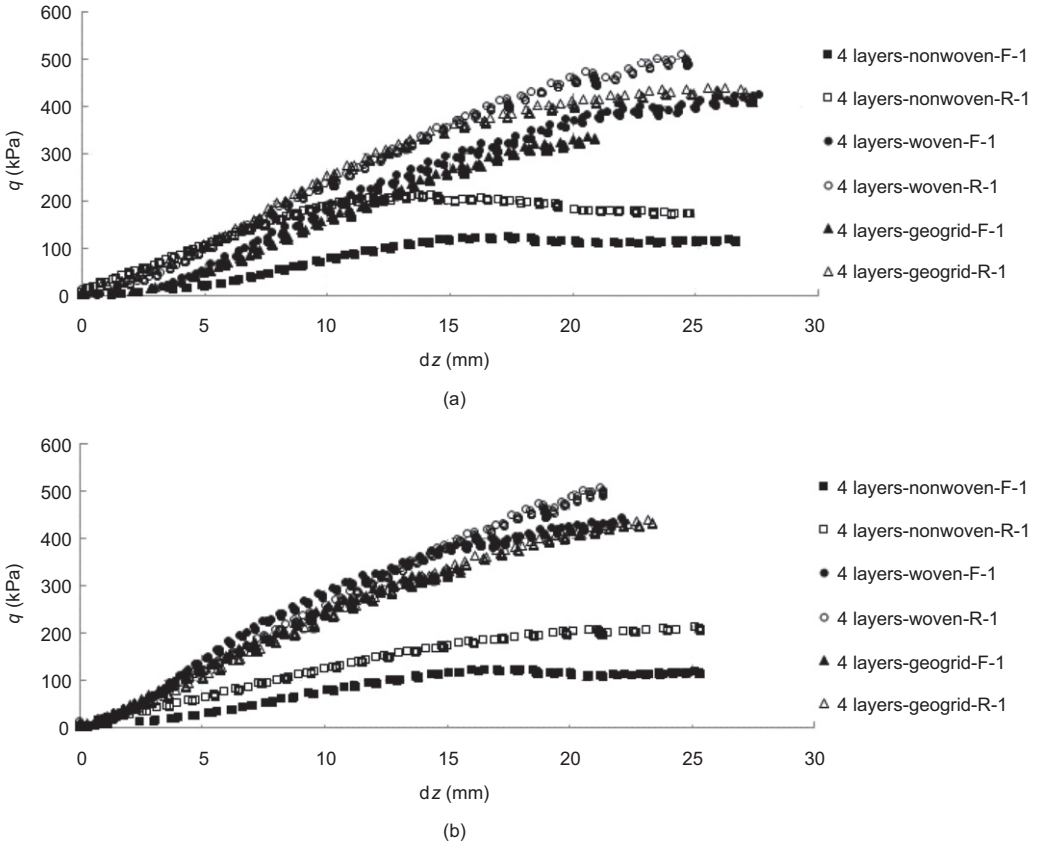

Figure 10. (a) Variations of q–dz; (b) q–dy relationship for reinforced backfill with four layers

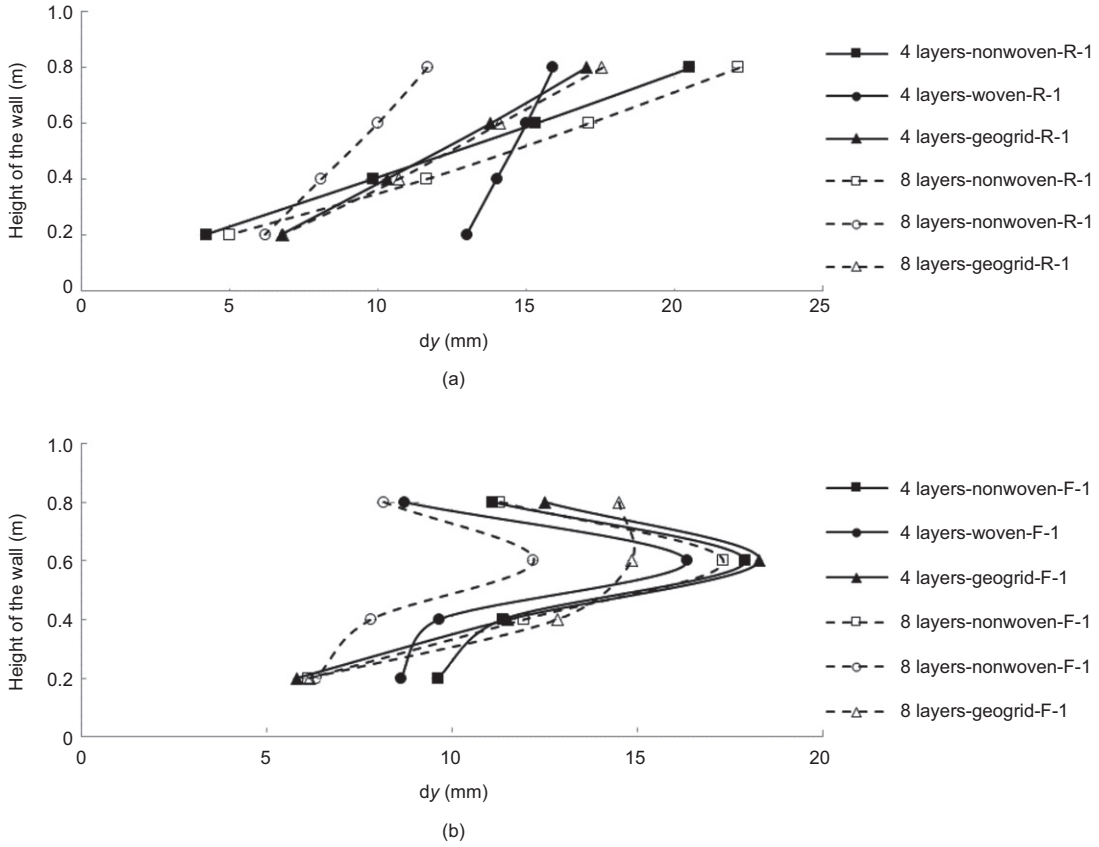

Figure 11. Lateral wall deflection after applying the same settlement in the strip footing (0.08B): (a) rigid face; (b) flexible face

friction angle; γ, the unit weight of the reinforced soil; H, the height of the wall and $\sigma_0 = (T_u/S_v)$ that T_u is ultimate tensile strength of the reinforcement and S_v is the vertical space between the reinforcement layers. For the model tests with four layers, $H = 0.8$ m, $b/a = 1.5$ and $\sigma_{01,2,3} = 50$, 75 and 37.5 kN/m and $\varphi = 40.5°$, the ultimate bearing capacity from Equation (2) will be 346, 522 and 258 kPa for fully flexible facing panel with geogrid, woven and nonwoven geotextiles, respectively (the overall flexural rigidity of the facing panel is not considered in this method).

Table 3 shows the comparison between the test results and this analytical method. From this table, the Sawicki and Lesniewska (1987) method shows higher calculated values for the ultimate bearing capacity than found in the tests especially for the models with the flexible face. This difference can be because of the considered fully mobilised interaction between the soil and reinforcement layers in the analytical method. In the ultimate state of this method, only the simultaneous rupture failure mechanism was considered for reinforcement layers, but from this study only the pull-out failure mechanism occurred. For the upper reinforcement layer, as there is less overburden pressure, the pull-out failure mechanism was noticed instead of rupture.

To consider the pull-out failure and the facing panel flexural effect, Ahmadi and Hajialilue (2012) developed an analytical method to calculate the ultimate load-bearing capacity of a strip footing located near a reinforced soil wall. Depending on the soil, reinforcement and facing panel properties in model tests, the ultimate bearing capacities of the strip footing are shown in Table 3.

There is good agreement between this method and the models with four layers. In models with eight layers, the difference is greater, as in this method the pull-out condition was considered in all reinforcement layers in the failure step.

4.3. Maximum wall deflection

Figures 11a and 11b show the curves of lateral wall deflection in the same footing settlement (0.08B) and for the rigid and flexible models, respectively. The measurements disregard the small deflections at the end of backfill construction (set to zero). For the flexible face, the maximum lateral wall deflection occurred in $z/H = 0.25$. For the same footing settlement (0.08B), the rigid and flexible wall with woven geotextile has the smallest wall deflection.

Table 4 shows the difference between the test results and Jewell (1988) method about the maximum wall deflection under the strip footing load. In the analytical methods, the (2V:1H) distribution for the strip footing load distribution in depth was considered to calculate the maximum tensile forces on reinforcement layers. In this table, for the highly extensible reinforcement layers (nonwoven geotextile), there is a significant difference between the test results and the Jewell (1988) method (almost 4–6 times).

For the stiffer reinforcement layers (geogrid and woven geotextile), the Jewell (1988) method shows better results compared to the model tests. It shows, by increasing reinforcement layers stiffness, the load distribution shape on reinforcement layers can be closer to the considered distribution in the Jewell (1988) method.

Table 3. The ultimate bearing capacity of the strip footing load for flexible (F) and rigid (R) facing

Test	*N*	Tests (kN/m^2)	Sawicki and Lesniewska (1987) (kN/m^2)	Ahmadi and Hajialilue (2012) (kN/m^2)
Four layers-nonwoven-F/R	4	120/204	258/258	173/212
Four layers-woven-F/R	4	306/390	522/522	339/415
Four layers-geogrid-F/R	4	277/375	346/346	245/301
Four layers-nonwoven-F/R	8	278/386	522/522	426/522
Four layers-woven-F/R	8	503/506	1051/1051	583/714
Four layers-geogrid-F/R	8	460/504	698/698	545/668

Table 4. Maximum wall deflection for the first loading and second loading steps at the ultimate load stage (dz = 0.08B and 0.04*B*)

Test	*N*	Tests (mm)	Jewell (1988) **method**	Jewell (1988) **modified method**
Four layers-nonwoven-F-1/R-1	4	16.5/20.3	60.1/100	-/-
Four layers-woven-F-1/R-1	4	11.8/15.5	10.9/13.7	-/-
Four layers-woven-F-2/R-2		5.5/7.1	-/-	4.1/5.2
Four layers-geogrid-F-1/R-1	4	13/17	13.2/18.2	-/-
Four layers-geogrid-F-2/R-2		6.1/8.5	-/-	5.1/7.2
Eight layers-nonwoven-F-1/R-1	8	17.3/22.1	101/140.3	-/-
Eight layers-nonwoven-F-2/R-2		7.8/10.8	-/-	33.8/46.8
Eight layers-woven-F-1/R-1	8	12.2/11.6	12.9/13.7	-/-
Eight layers-woven-F-2/R-2		5.5/4.6	-/-	4.7/4.4
Eight layers-geogrid-F-1/R-1	8	14.9/16.1	16.7/18.3	-/-
Eight layers-geogrid-F-2/R-2		7.2/7.8	-/-	6.2/6.7

4.4. Preloading effect on MSE walls deflection

Tatsuoka *et al.* (1997) and Uchimura *et al.* (2003) proposed the pre-loaded and pre-stressed reinforced soil method in the abutment of geogrid. The transient and long-term residual deformations measured in the wall after pre-loading were reported to be very small. Ehrlich and Mitchell (1995) indicated that the induced stress due to soil compaction (pre-loading) may represent a kind of pre-stressing and reduce lateral displacement after wall construction.

In the model tests, after unloading the strip footing load, a second load (reloading) was applied to models, to study the effect of the preloading on the wall deflection under the strip footing load. The lateral wall deflections after applying the second loading step for the flexible and rigid walls with geogrid reinforcement are shown in Figure 12. From this figure, the measured footing settlements in the second loading step are smaller than the first loading step, because of the preloading effect on reinforcement layers from the first loading step.

The over-consolidation effect on the lateral earth pressure (and consequently reinforcement layers tensile load) can be considered by applying the value of the F parameter, based on Seed (1983) and Ehrlich and Mitchell (1994) formula, as

$$F = 1 - \frac{\mathrm{OCRR} - \mathrm{OCRR}^{\sin\varphi}}{\mathrm{OCRR} - 1} \quad (3)$$

where OCRR and φ are the over-consolidation ratio in a retained soil structure (i.e. defined as the highest stress experienced divided by the current stress) and internal peak friction angle of soil, respectively.

There is good agreement between the Jewell (1988) method with the test results in the second loading step by considering the preloading effect (the average value of the F parameter) for stiffer reinforcement layers. But still there is a significant difference between the test results and the Jewell (1988) method for the models with nonwoven geotextile layers under the second loading step.

4.5. Nonwoven geotextile stiffness

Yuan *et al.* (1998) and Wilson-Fahmy *et al.* (1993) from the test results showed that soil confinement had a negligible effect on the modulus for the woven geotextile, and for the nonwoven geotextiles tested the modulus increased 1.8 to 4.8 times depending on the confining stress. Moreover, Zornberg (1994) with back analysis in the numerical modelling of full-scale test results showed that *in situ* nonwoven geotextile stiffness was found to vary from twice to four times the values determined from the laboratory unconfined wide width tensile tests. Palmeira (2009) has also reported the effect of confinement for nonwoven geotextile stiffness by increasing the interlock and friction among geotextile fibres and intrusion of soil particles into geotextile voids (impregnation), which reduces the space available for fibre stretching.

PIV analysis can help to get more information about the strain distribution on the reinforcement layers' location. Figures 13a–13h shows the distribution of strains in eight layers of nonwoven geotextile (flexible face) and for the first loading step. From this figure, the maximum strain occurs in the second layer and the distribution is different from the Jewell (1988) method. The strain distribution is similar to the triangle shape considered in the Ahmadi and Bezuijen (2018) study and it occurs almost in the area with the angle $(\pi/4 + \varphi/2)$ under the strip footing load. As shown in Figure 13, the maximum strain for the second layer is localised in the small part exactly under the strip footing load (because of the low stiffness of nonwoven geotextile and the texture of needle-punched material, the maximum strain occurred in the small part and is not continued throughout the length of the reinforcement layer). By considering the triangle shape with the maximum strain value of 10% in the second layer, as shown in Figure 13b, the maximum wall deflection will be 15 mm and this is comparable with the measured value (17.3 mm). From the AASHTO (2012) method, the maximum tensile force on the second reinforcement layer is 3.4 kN/m and, from the tensile test curve in Figure 3, the equivalent strain for this maximum tensile load will be 35%. Then, the PIV analysis results on average showed 3.5 times smaller strain over the reinforcement layer than the calculated value. This shows the influence of the interaction mechanism on the stiffness of nonwoven geotextile. From Figure 13, the measured maximum strain decreases by increasing the depth, and the location of the maximum strain over the

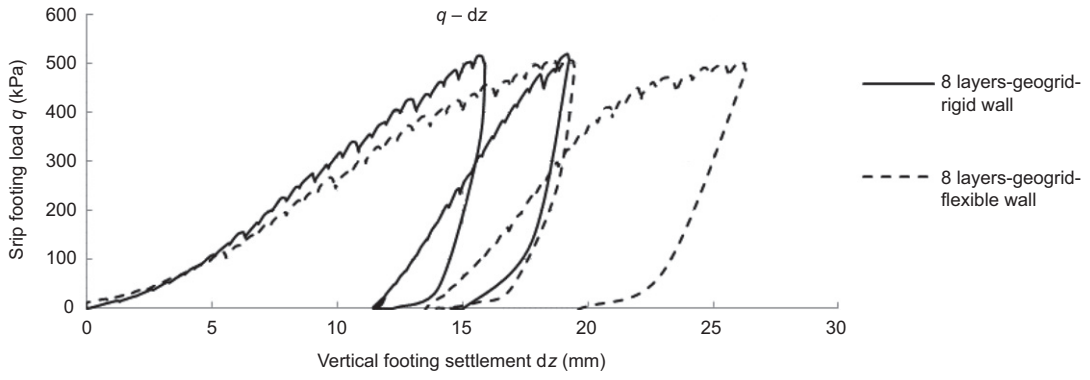

Figure 12. Strip footing load versus vertical footing settlement for geogrid reinforcement layers in the first loading and second loading steps

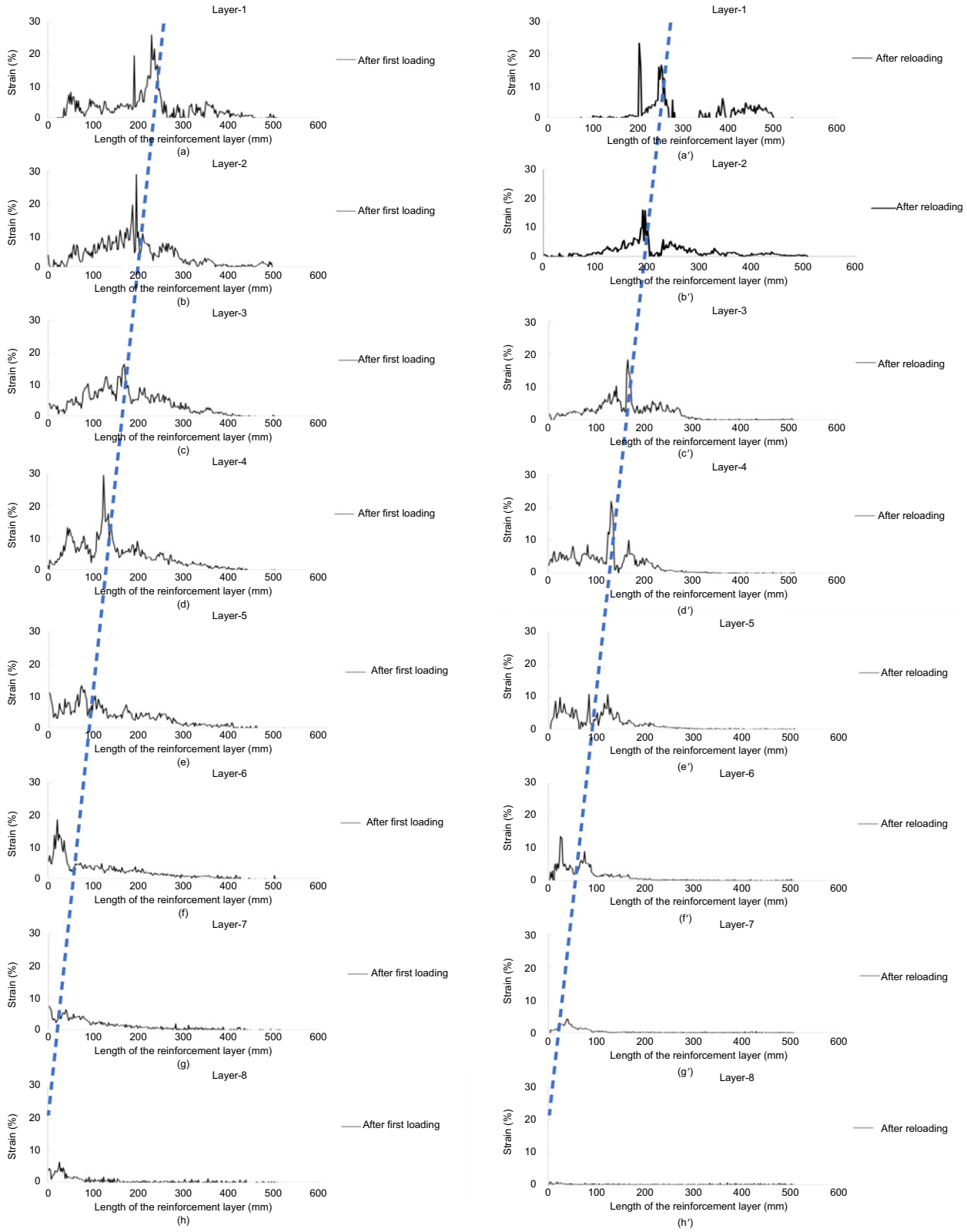

Figure 13. Strain distribution on the reinforcement layers location from the PIV analysis in the first and second loading steps and in the test with eight layers nonwoven geotextile, flexible wall; a to h and a′ to h′) from first to eighth layer

reinforcement layers moves to the wall face in the lower reinforcement layers.

Figures 13a′–13h′ show the strain distribution over the reinforcement layers in the second loading step. From this figure, the strain distribution is different from the first loading step and the maximum strain and the interacted length are smaller. For the second layer, the strain distribution is located in the failure area with the angle $(\pi/4 + \varphi/2)$ but with a smaller interacted length compared to the first loading step in Figure 13b. By integration of the strain distribution curve on the second reinforcement layer in Figure 13b′, the wall deflection will be 9.2 mm;

that is comparable with the measurement (10.8 mm). The last reinforcement layer (eighth) shows a very small strain increment in the second loading step and the location of the maximum strain over the reinforcement layers in this figure moves to the wall face, similar to the first loading step.

5. COMPARISON OF MODEL RESULTS WITH THOSE OF FULL-SCALE MODELS

The structures evaluated as part of this study correspond to reduced-scale models, with a scale factor of 1/5 of the full-scale structures evaluated by Ahmadi and Bezuijen (2018). The same scale factor (1/5) was used both for the geometric dimensions (i.e. size) of the model and the reinforcement stiffness. The same pressure from strip footing loads was applied on the backfill of the small-scale models as that used in the full-scale structures.

El-Emam and Bathurst (2004) and Xu *et al*. (2020) used a scale factor of 1/6 and 1/5 respectively to investigate the seismic performance of reduced-scale reinforced soil walls. Based on Allen and Bathurst (2019), Allen and Bathurst (2015) and Miyata *et al*. (2018) studies, the range of global stiffnesses for geosynthetic walls in the full-scale tests are (75–9222 kPa). In this study, and for the small-scale models with four and eight reinforcement layers, the global stiffness is in the range of full-scale tests (75–2300 kPa).

Among the different sets of small-scale models, those with eight geogrid layers correspond to the models with a scale factor of 1/5 in relation to the full-scale structures. Table 5 shows a comparison between the results obtained in the reduced-full-scale structures, including the soil parameters, reinforcement characteristics, and test results. As inferred from the results summarised in this table, the maximum wall deflections in the reduced-scale models constructed with eight geogrid layers in the first loading step are 10.3 and 11 mm for a surcharge load of 300 kPa in the rigid and flexible walls, respectively. Evaluation of the results indicates that the displacement values of the small and full-scale models compare particularly well before the preloading that was conducted in the full-scale models. However, the difference between the displacement values of scaled and full-scale models are significant (4.6 to 4.9 times in rigid and flexible walls) for the second loading step (i.e. close to the scale factor of 1/5 in small-scale models).

A preloading effect from roller compactor (Dynapac CA302) as a localised load was observed in the full-scale structures before applying a 300 kPa static strip footing load. Based on Seed (1983) and Duncan and Seed (1986), the loading imposed by a typical vibratory roller can be modelled by applying a static load that is approximately two to four times the weight of the roller. In fact, when considering a static vertical stress equivalent to four times that of the roller compactor (432 kPa per unit width of the reinforced wall), a good comparison could be obtained between the results in the full-scale structure and those in the second loading step in small-scale tests (that can show the preloading effect in both models).

Finally, by mobilising the reinforcement layers under the preloading mechanism from the dynamic or static loads, the maximum lateral wall deflection will decrease both in full-scale and small-scale models. This mobilisation can be achieved by the preloading effect of a dynamic roller compactor or by a static load in the same position.

While important insight can be gained from 1 g models regarding mechanisms involved in new approaches such as the preloading of MSE, it is important to also highlight the limitations of reduced-scale models in reproducing the overall behaviour of full-scale prototype structures. In particular, the impact of stress dependency on the soil properties cannot be reproduced in the reduced-scale model for the case of stresses induced by the self-weight of a geotechnical structure. In this particular study, this deficiency was addressed, at least partly, because the magnitude of the surcharge-induced stresses dominates the overall state of stresses within the reinforced soil mass. Specifically, the stresses in the model are induced by comparatively large strip footing loads. Nonetheless,

Table 5. Soil and reinforcement parameters in full and small-scale tests

Parameter	Full-scale test	Small-scale test
Unit weight-soil (kN/m^3)	17.3	15.7
Peak soil friction angle from the triaxial test (°)	39.09	40.5
Residual friction angle from the triaxial test (°)	35.1	31.3
Soil dilation angle from the test (°)	12.5	11.7
Cohesion-soil (kPa)	0	0
Reinforcement length (m)	3	0.6
Height of the wall (m)	4	0.8
Vertical spacing of reinforcement (m)	0.25 and 0.50	0.05 and 0.1
Long term (1000 h) stiffness of reinforcements ($\varepsilon \leq 0.5\%$) (kN/m)	670	—
Short-term (1 h) stiffness of reinforcements (kN/m)	700	150
Strip footing load (kN/m^2)	Up to 300	Up to 500
Width of the strip footing load (m)	1	0.2
Rigid wall deflection under the 300 kPa load (mm) first loading step in small-scale test	12.1	10.3
Flexible wall deflection under the 300 kPa load (mm) first loading step in small-scale test	16.2	11
Rigid wall deflection under the 300 kPa load (mm) second loading step (after unloading 500 kPa)	—	2.6
Flexible wall deflection under the 300 kPa load (mm) second loading step (after unloading 460 kPa)	—	3.3

stresses in the geosynthetics located comparatively far from the footing in the reduced-scale models may be reasonably different than those in a full-scale prototype. However, the focus of this study is on gaining insight on preloading as an advantageous methodology, such insight will add to our current knowledge base on this topic, particularly since footing pressures in this study are the same in the small-scale model as in the prototype.

6. CONCLUSIONS

This paper presents a series of instrumented scaled models by considering the influence of facing panel rigidity, stiffness of the reinforcement layers and preloading on the lateral wall deflection, strip footing settlement, vertical earth pressure and, consequently, the maximum tensile force in the reinforcement layers. Furthermore, the measurements are compared with the results of analytical methods about the bearing capacity of strip footing load and maximum wall deflection. PIV analysis results in this study provided measurements of failure zones inside the soil, before and after applying the strip footing load, that illustrate the effect of facing panel rigidity, stiffness of the reinforcement layers and preloading on the related system behaviour.

As mentioned before, preloading is induced by the strip footing load, which increases the soil density and horizontal stresses. A consequence of the increment in horizontal stresses is the elongation of the reinforcement layers. After unloading the strip footing, the tensile force in the reinforcement layer in the elastic range will result in an added confinement within the soil. The induced tensile force from the first loading can partly result in soil upward movements, but the primary effect is a pre-stressed force. On the other hand, the first loading step can activate the reinforcement layers within the soil mass by decreasing the displacements needed to mobilise the maximum frictional and bearing resistance in the longitudinal and transverse ribs.

Then, in a new approach to study the deformation of MSE walls, a preloading is applied to simulate the densification of the soil layers. This densification will activate the reinforcement layers inside the soil and decrease the large necessary displacement for mobilisation of the ultimate bearing and friction resistance. A localised static or dynamic surcharge load close to the facing panel can be used as a preloading to mobilise the reinforcement layers inside the soil and prestresses them. Due to this prestressing, the wall deflection and strip footing settlement under the future surcharge loads will be less than without considering this pre-stressing condition (depending on the magnitude of the first applied load).

(1) The vertical soil pressure in loading and reloading steps was found to decrease more than predicted by typical design methods for increasing facing rigidity and decreasing reinforcement stiffness.
(2) The total maximum wall deflection induced during the second loading was almost half the value reached during the first loading. In addition, the footing settlement induced during the second loading was also smaller than that obtained during the first loading.
(3) Evaluation of the results indicates that the displacement values of the small and full-scale models compare particularly well after the preloading that was conducted in the full-scale models. The measured maximum wall deflection in small-scale models and in the second loading step has the scale factor of 1/5 compared to the full-scale models.
(4) Increasing wall face rigidity and reinforcement stiffness were found to lead to decreased lateral wall deflections and footing settlements. On the other hand, the bearing capacity of strip footing increases by increasing the wall face rigidity and reinforcement stiffness.
(5) The models constructed with a comparatively rigid facing resulted in failure zones that initiated at a lower elevation on the facing than for the case of models with a more flexible facing. That is, application of strip footing loads led to a deeper failure zone when using rigid facing than in the case of flexible facing.
(6) In the rigid wall compared to the flexible wall, there is a clear shear zone generated close to the wall face in the vertical direction (soil-wall face frictional interaction).
(7) The results from PIV analysis revealed that two failure lines with the angle $(\pi/4 + \varphi/2)$ formed under the strip footing load in the loading and reloading steps. Specifically, a surface developed from the inner edge of the strip footing and with a tendency to the wall face (shallow position) while a second one developed from the outer edge of the strip footing (deep position).
(8) PIV analysis results showed that the strain distribution presents a triangular shape on the models with rigid and flexible faces for nonwoven geotextile and under the strip footing load.
(9) For the reinforcement layers with only frictional interaction (nonwoven and woven geotextiles), the failure zones are deeper than for the layers with bearing and frictional resistance (geogrid). In geogrid layers, more displacement is needed to get the maximum bearing resistance of the transverse ribs.
(10) Good agreement between analytical predictions and experimental results were obtained in the loading and reloading step.
(11) The maximum strain value from PIV analysis and for the nonwoven geotextile is smaller than the value obtained through the AASHTO (2012) method, reflecting the influence of the confinement on the stiffness of this type of reinforcement.
(12) Compared to AASHTO (2012) and FHWA (2009), the failure zone defined using PIV analysis is shown

to reach the wall face at a location above the toe of the wall, which is adopted in those guidelines. This may have implications not only on the locus of the maximum tension in the reinforcements but also in the magnitude of such maximum tension.

(13) By considering the preloading effect, the necessary stiffness of the reinforcement layers designed for the surcharge loads can be decreased, because the preloading leads to a stiffer behaviour. This means a single loading-unloading cycle with the same magnitude as the future surcharges may have the same effect on the wall deflection and footing settlement by using two times stiffer reinforcement layers.

(14) The results show that the maximum wall deflection for the flexible facing panel and under the first and second loading of strip footing load occurred in $z/H = 0.25$, which is in good agreement with the full-scale tests of Abu-Hejleh *et al*. (2002) and Ahmadi and Bezuijen (2018).

ACKNOWLEDGEMENT

The authors appreciate the help of the Iranian Ministry of Science, Research and Technology and CWO (Ghent University funding) for financial support.

APPENDIX A. PROCEDURE OF THE ANALYTICAL METHOD BY AHMADI AND HAJIALILUE-BONAB (2012) FOR CALCULATING THE ULTIMATE LOAD-BEARING CAPACITY UNDER STRIP FOOTING LOCATED NEAR THE REINFORCED SOIL WALLS

By considering the facing panel rigidity, Ahmadi and Hajialilue (2012) developed an analytical method for calculating the ultimate load-bearing capacity under a strip footing load located near the reinforced soil walls. In this model, the ultimate strip footing load (q_r) can be described as:

$$q_{\mathrm{r}} = \frac{1}{\bar{W}_{\mathrm{q}}} \cdot \left(\frac{(1+\xi) M_{\mathrm{R}}}{x \tan\theta_{\mathrm{f}} \left(\xi - \xi^2\right)} + \sum_{i=1}^{n} T_{\mathrm{p}} \cdot L_i - \bar{W}_{\gamma} \right) \quad (4)$$

where L_i (the perpendicular depth of the ith reinforcement layer) is measured downwards from the centre of rotation (O); T_p is the pull-out resistance force of the ith layer; N is the number of the reinforcement layers.

$$\bar{W}_q = \int_{\theta_0}^{\theta_f} \frac{x}{(\tan\theta_f - \tan\theta_0)} \times \frac{(\tan\theta_f - \tan\theta) \cdot (\tan\theta - \tan\phi)}{\sin\theta \cdot \cos\theta} \times \mathrm{e}^{-2\theta \cdot \tan\phi} \cdot \mathrm{d}\theta \quad (5)$$

$$\bar{W}_{\gamma} = \int_{\theta_0}^{\theta_f} \frac{x^2 \cdot \gamma}{\left(\tan\theta_f - \tan\theta_0\right)} \cdot \frac{\left(\tan\theta_f - \tan\theta\right) \cdot (\tan\theta - \tan\phi)}{\cos^2\theta} \left(3\tan\phi \cdot \cos\theta + \sin\theta - 3\tan\phi \cdot \mathrm{e}^{-3\theta \cdot \tan\phi}\right) \cdot \mathrm{d}\theta \quad (6)$$

$$\cos\theta_0 = \mathrm{e}^{-\theta_0 \cdot \tan\phi} \quad (7)$$

Other parameters are shown in Figure 14 and more details are provided by Ahmadi and Hajialilue (2012).

Assuming a friction coefficient between the reinforcement and the soil defined by μ, the pull-out force resistance can be calculated as

$$T_p = 2 \cdot l_e \cdot \gamma \cdot z \cdot \mu \quad (8)$$

By considering the soil and facing panel properties from the small-scale tests with four layers of geogrid, the parameters in this method will be $x = 0.059$, $\theta_0 = 1.19$ (rad) and $\theta_f = 1.48$ (rad), then the ultimate bearing capacity of strip footing for four layers of geogrid when $M_r = 0$ (without facing resistance) is 228 kPa. For the

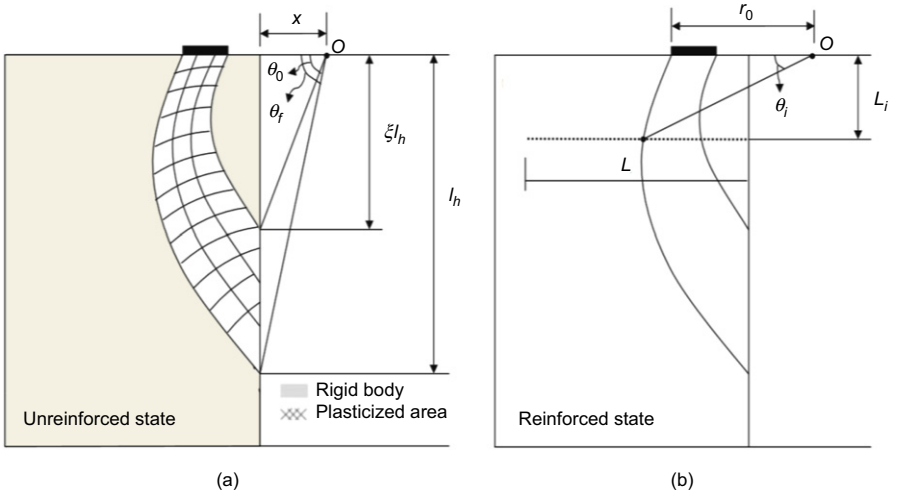

Figure 14. Failure mechanism and parameters for analytical analysis (Ahmadi and Hajialilue-Bonab 2012)

plywood, the maximum bending resistance is considered from

$$M_r = \sigma_y \times S \tag{9}$$

where, σ_y is tensile strength and $S = wt^2/6$ is the moment inertia of the section with width (w) and height (t). For plywood, $\sigma_y = 31$ MPa, $S = 1.2 \times 10^{-6}$ m^3, then M_r will be 0.037 kN.m. Then the ultimate bearing capacity of strip footing load based on this method for four layers of geogrid when $\mu = 1$ and $\xi = 0.31$ (from the PIV result) and for the flexible wall will be 245 kPa.

As the rigid face has a reasonably high bending capacity also to be overcome by the strip footing load, the maximum amount for M_r can be calculated from the q_r formula based on the assumption that with this M_r, the top reinforcement layer would fail by pull out. Accordingly, $M_r = 1.51$ kN.m and the ultimate bearing capacity for strip footing for 4 layers of geogrid will be 301.08 kPa for the rigid face.

NOTATION

Basic SI units are shown in parentheses.

- a strip footing load width (m)
- B width of strip load (m)
- b distance between load and wall (m)
- C cohesion-soil (kPa)
- C_c coefficient of curvature (dimensionless)
- C_u coefficient of uniformity (dimensionless)
- dz strip footing settlement (m)
- dy lateral wall deflection (m)
- E_1A short-term stiffness of geogrid (kN/m)
- E_2A short-term stiffness of woven geotextile (kN/m)
- E_3A short-term stiffness of nonwoven geotextile (kN/m)
- H height of wall (m)
- h vertical space between reinforcement layers (m)
- L reinforcement length (m)
- L_i perpendicular depth of ith reinforcement layer (m)
- l_e effective length of reinforcement layer (m)
- M_r cross section moment of resistance (kN.m)
- N number of reinforcement layers (dimensionless)
- OCRR over-consolidation ratio in a retained soil structure (dimensionless)
- q strip footing load (kPa)
- q_r ultimate strip footing load (kPa)
- q_v vertical stress in the depth (kPa)
- S moment inertia of the section (m^3)
- S_v vertical space between reinforcement layers (m)
- T_p pull-out resistance force of the ith layer (kN/m)
- T_u ultimate tensile strength of reinforcement (kN/m)
- T_{u1} ultimate tensile strength of geogrid (kN/m)
- T_{u2} ultimate tensile strength of woven geotextile (kN/m)
- T_{u3} ultimate tensile strength of nonwoven geotextile (kN/m)
- t height of the section (m)
- u vertical distance from the soil surface (m)
- w width of the section (m)
- z vertical distance from soil surface (m)
- γ unit weight of reinforced soil (kN/m^3)
- γ_s unit weight-soil (kN/m^3)
- μ friction coefficient between the reinforcement and the soil (dimensionless)
- σ_0 ratio of the ultimate tensile strength of reinforcement to the vertical space between reinforcement layers (kN/m^2)
- σ_y tensile strength (kPa)
- φ soil friction angle in a retained soil structure (degrees)
- φ_d peak soil friction angle from the direct shear test (degrees)
- φ_p estimated soil plain strain friction angle (Bolton 1986) (degrees)
- φ_r residual friction angle from the direct shear test (degrees)

REFERENCES

AASHTO (2012). *LRFD Bridge Design Specifications*, 6th edn. American Association of State Highway and Transportation Officials, Washington, DC, USA.

Abu-Hejleh, N., Zornberg, J. G., Wang, T. & Watcharamonthein, J. (2002). Monitored displacements of unique geosynthetic-reinforced soil bridge abutments. *Geosynthetics International*, **9**, No. 1, 71–95.

Adams, M. (1997). Performance of a prestrained geosynthetic reinforced soil bridge pier. In *Mechanically Stabilized Backfill*, Wu, J. T. H., Editor, Balkema, Rotterdam, the Netherlands, pp. 35–53.

Adams, M., Nicks, J., Stabile, T., Wu, J., Schlatter, W. & Hartmann, J. (2011). *Geosynthetic Reinforced Soil Integrated Bridge System Interim Implementation Guide*, FHWA-HRT-11-026. U.S. Department of Transportation, Washington, DC, USA.

Ahmadi, H. (2020). *Geosynthetic-reinforced Soil Retaining Walls Subjected to Surcharge Loads*. Ph.D. dissertation, Ghent University, Ghent, Belgium, 180p.

Ahmadi, H. & Bezuijen, A. (2018). Full-scale mechanically stabilized earth (MSE) walls under strip footing load. *Geotextiles and Geomembranes*, **46**, No. 3, 297–311.

Ahmadi, H. & Hajialilue-Bonab, M. (2012). Experimental and analytical investigations on bearing capacity of strip footing in reinforced sand backfills and flexible retaining wall. *Acta Geotechnica*, **7**, No. 4, 357–373.

Allen, T. M. & Bathurst, R. J. (2015). An improved simplified method for prediction of loads in reinforced soil walls. *ASCE Journal of Geotechnical and Geoenvironmental Engineering*, **141**, No. 11, 04015049.

Allen, T. M. & Bathurst, R. J. (2019). Geosynthetic reinforcement stiffness characterization for MSE wall design. *Geosynthetics International*, **25**, No. 6, 592–610.

Bathurst, R. J. (2020). Developments in MSE wall research and design. In *Innovative Infrastructure Solutions Using Geosynthetics, GeoMEast 2019, Cairo, Egypt, Sustainable Civil Infrastructures*, Tatsouka, F., Guler, E., Shehata, H. & Giroud, J., Editors, Springer, Cham, Switzerland, pp. 22–50.

Bolton, M. D. (1986). The strength and dilatancy of sands. *Geotechnique*, **36**, No. 1, 65–78, https://doi.org/10.1680/geot.1986.36.1.65.

Bourgeois, E., Soyez, L. & Le Kouby, A. (2011). Experimental and numerical study of the behaviour of a reinforced-earth wall subjected to a local load. *Computers and Geotechnics*, **38**, No. 4, 515–525.

Brabant, K. (2001). *Mechanically Stabilized Earth Walls for Support of Highway Bridges*. The Reinforced Earth Company, Unpublished Report.

Coulomb, C. A. (1776). *Essai sur une Application des Regles de Maximis et Minimis A Quelqes Problemas de Stratique Relatifs A L'architecture. Memoires de Mathematique et de Physique. Presentes A L'Academie Royale des Sciences*, De l'Imprimerie Royale, Paris, France, vol. 7, pp. 343–382.

Damians, I. P., Bathurst, R. J., Josa, A. & Lloret, A. (2014). Numerical study of the influence of foundation compressibility and reinforcement stiffness on the behavior of reinforced soil walls. *International Journal of Geotechnical Engineering*, **8**, No. 3, 247–259.

Duncan, J. M. & Seed, R. B. (1986). Compaction-induced earth pressures under K0-conditions. *Journal of Geotechnical Engineering*, **112**, No. 1, 1–22.

Ehrlich, M. & Mitchell, J. K. (1994). Working stress design method for reinforced soil walls. *Journal of Geotechnical Engineering*, **120**, No. 4, 625–645.

Ehrlich, M. & Mitchell, J. K. (1995). Working stress design method for reinforced soil walls. Closure. *Journal of Geotechnical Engineering*, **121**, No. 11, 820–821.

El-Emam, M. & Bathurst, R. J. (2004). Experimental design, instrumentation and interpretation of reinforced soil wall response using a shaking table. *International Journal of Physical Modelling in Geotechnics*, **4**, No. 4, 13–32.

FHWA (Federal Highway Administration) (2009). *Design of Mechanically Stabilized Earth Walls and Reinforced Slopes*, Rep. No. FHWA-NHI-10-024 Vol. I and NHI-10-025 Vol. II. Federal Highway Administration, 306 Vol. 1 and 378 Vol. 2, Washington, DC, USA.

Gotteland, P., Gourc, J. P. & Villard, P. (1997). Geosynthetic reinforced structures as bridge abutments: full scale experimentation and comparison with modelisations. In *Mechanically Stabilized Backfill*, Wu, J. T. H., Editor, Balkema, Rotterdam, the Netherlands, pp. 25–34.

Ho, S. K. & Rowe, R. K. (1996). Effect of wall geometry on the behavior of reinforced soil walls. *Geotextiles and Geomembranes*, **14**, No. 10, 521–541.

Jewell, R. A. (1988). Reinforced soil wall analysis and behavior. In *The Application of Polymeric Reinforcement in Soil Retaining Structures*, Jarrett, P. M. & McGown, A., Editors, Springer, Dordrecht, the Netherlands, pp. 365–408.

Ketchart, K. & Wu, J. T. H. (1997). Performance of geosynthetic-reinforced soil bridge pier and abutment. *International Symposium on Mechanically Stabilized Backfill, Special Presentation*, Denver, CO, USA, Wu, J. T. H., Editor, Balkema, Rotterdam, the Netherlands, pp. 101–116.

Lackner, C., Bergado, D. T. & Semprich, S. (2013). Prestressed reinforced soil by geosynthetics-concept and experimental investigations. *Geotextiles and Geomembranes*, **37**, 109–123.

Lee, K. Z. Z. & Wu, J. T. H. (2004). A synthesis of case histories on GRS bridge-supporting structures with flexible facing. *Geotextiles and Geomembranes*, **22**, No. 4, 181–204.

Lesniewska, D. & Wood, D. M. (2009). Observations of stresses and strains in a granular material. *Journal of Engineering Mechanics*, **135**, No. 9, pp. 1038–1054.

Miyata, Y., Bathurst, R. J. & Allen, T. M. (2018). Evaluation of tensile load model accuracy for PET strap MSE walls. *Geosynthetics International*, **25**, No. 6, 656–671.

Palmeira, E. M. (2009). Soil-geosynthetic interaction: modeling and analysis. *Geotextiles and Geomembranes*, **27**, No. 5, 368–390.

Plumey, S., Muttoni, A., Vulliet, L. & Labiouse, V. (2011). Analytical and numerical analyses of the load-bearing capacity of retaining walls laterally supported at both ends. *International Journal for Numerical and Analytical Methods in Geomechanics*, **35**, No. 9, 1019–1033.

Rowe, R. K. & Ho, S. K. (1997). Continuous panel reinforced soil walls on rigid foundations. *Journal of Geotechnical and Geoenvironmental Engineering*, **123**, No. 10, 912–920.

Ruiken, A., Ziegler, M., Vollmert, L. & Duzic, I. (2010). Recent findings about the confining effects of geogrids from large scale laboratory testing. *9th International Conference on Geosynthetics*, IGS Brasil, Sao Paulo, Brazil, pp. 691–694.

Sawicki, A. & Lesniewska, D. (1987). Failure modes and bearing capacity of reinforced soil retaining walls. *Geotextiles and Geomembranes*, **5**, No. 1, 29–44.

Schlosser, F. & Bastick, M. (1991). Reinforced earth. In *Foundation Engineering Handbook*, 2nd edn. Fang, H.Y., Editor, Chapman & Hall, New York, NY, USA, pp. 778–795.

Seed, R. M. (1983). *Compaction-induced Stresses and Deflections on Earth Structure*. Ph.D. thesis, University of California, Berkeley, CA, USA, 447p.

Tatsuoka, F. (1992). Roles of facing rigidity in soil reinforcing. *Keynote Lecture, Proc. Earth Reinforcement Practice*, Fukuoka, Japan, Ochiai, H., Hayashi, S. & Otani, J., Editors, Balkema, Rotterdam, the Netherlands, pp. 831–870.

Tatsuoka, F., Uchimura, T. & Tateyama, M. (1997). Preloaded and pre-stressed reinforced soil. *Soils and Foundations*, **37**, No. 3, 79–94.

Teixeira, S. H. C., Benedito, S. B. & Zornberg, J. G. (2007). Pull-out resistance of individual longitudinal and transverse geogrid ribs. *Journal of Geotechnical and Geo-Environmental Engineering*, **133**, No. 1, 37–50.

Uchimura, T., Tateyama, M., Tanaka, I. & Tatsuoka, F. (2003). Performance of a preloaded-prestressed geogrid-reinforced soil pier for a railway bridge. *Soils and Foundations*, **43**, No. 6, 155–171.

White, D. J., Take, W. A. & Bolton, M. D. (2001). Measuring soil deformation in geotechnical models using digital images and PIV analysis. *Proceedings of 10th International Conference on Computer Methods and Advances in Geomechanics*, Tucson, AZ, USA, Chandra, S. D., Editor, Balkema, Rotterdam, the Netherlands, pp. 997–1002.

White, D. J., Take, W. A. & Bolton, M. D. (2003). Soil deformation measurement using particle image velocimetry (PIV) and photogrammetry. *Geotechnique*, **53**, No. 7, 619–631.

White, D. J., Randolph, M. & Thompson, B. (2005). An image-based deformation measurement system for the geotechnical centrifuge. *International Journal of Physical Modelling in Geotechnics*, **5**, No. 3, 1–12.

Wilson-Fahmy, R. F., Koerner, R. M. & Fleck, J. A. (1993). Unconfined and confined width tension testing of geosynthetics. Geosynthetic soil reinforcement testing procedures. *ASTM STP*, **1190**, 49–63.

Wu, J. T. H., Ketchart, K. & Adams, M. (2001). *GRS bridge Piers and Abutments*, Rep. No. FHWA-RD-00-038. U.S. Department of Transportation, Washington, DC, USA.

Xiao, C., Han, J. & Zhang, Z. (2016). Experimental study on performance of geosynthetic-reinforced soil model walls subjected to static footing loading. *Geotextiles and Geomembranes*, **44**, No. 1, 81–94.

Xu, P., Hatami, K. & Jiang, G. (2020). Shaking table study of the influence of facing on reinforced soil wall connection loads. *Geosynthetics International*, **27**, No. 4, 364–378.

Yuan, Z., Swan Jr., R. H. & Bachus, R. C. (1998). Soil confinement effect on stress-strain properties of geosynthetics. *Proceedings of the Sixth International Conference on Geosynthetics*, Atlanta, GA, USA, Industrial Fabrics Association International, IFAI, Roseville, MN, USA, pp. 523–528.

Zornberg, J. G. (1994). *Performance of Geotextile-Reinforced Soil Structures*. Ph.D. dissertation, University of California, Berkeley, CA, USA, 504p.

Zornberg, J. G., Morsy, A. M., Mofarraj, B., Christopher, B. R., Leshchinsky, D., Han, J., Tanyu, B. F., Gebremariam, F. T., Shen, P. & Jiang, Y. (2019). *Proposed Refinements to Design Procedures for Geosynthetic Reinforced Soil (GRS) Structures in AASHTO LRFD Bridge Design Specifications*. National Cooperative Highway Research Program (NCHRP), Project 24-41. Transportation Research Board, Washington, DC, USA, March, 64pp.

The Editor welcomes discussion on all papers published in Geosynthetics International. Please email your contribution to discussion@geosynthetics-international.com by 15 December 2021.